

Impedance-Tuned Microwave Loop for Fast, Homogeneous Rabi Oscillations of a Dense Ensemble of NV-Diamond Electronic Spins

Han Sae Jung,[○] Johannes Cremer,[○] Aoyang Zhang,[○] Shuhao Fan, Sangha Kim, Guang Yang, Ronald L. Walsworth,^{*} and Donhee Ham^{*}



Cite This: *Nano Lett.* 2025, 25, 15566–15571



Read Online

ACCESS |



Metrics & More



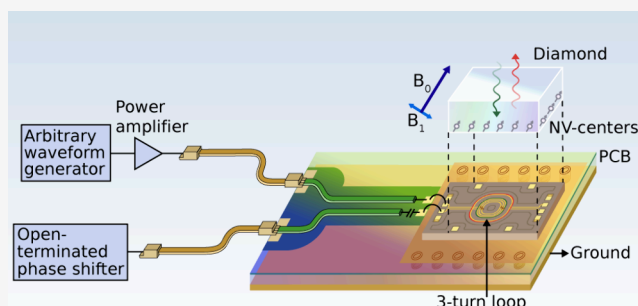
Article Recommendations



Supporting Information

ABSTRACT: Obtaining a high Rabi oscillation frequency homogeneously across a spatially extended population of nitrogen-vacancy (NV) center electronic spins in diamond is useful for efficient spin-state manipulation of the NV ensemble and in using NVs to detect ensembles of other spin species. Here, we achieve a high, homogeneous Rabi frequency for a dense NV ensemble by enhancing the microwave magnetic fields in the center region of a diamond-coupled planar metallic loop via systematic engineering that increases the microwave current driving of the loop, while avoiding off-center proximity to the loop that gives strong but inhomogeneous microwave fields. With such enhanced microwave fields at 2.55 GHz, we achieve a 136.3 MHz NV Rabi frequency with 1.5% inhomogeneity over a $40 \mu\text{m} \times 40 \mu\text{m}$ diamond area, and we use the NV ensemble to detect a ~ 30 -MHz magnetic signal, similar to a nuclear magnetic resonance (NMR) signal at a tesla-scale bias magnetic field, with Hz-scale spectral resolution.

KEYWORDS: Nitrogen-vacancy center, diamond, electron spins, Rabi oscillation, quantum coherence, microwave engineering, nuclear magnetic resonance



Electronic spin dynamics in diamond nitrogen-vacancy (NV) centers can have sufficient quantum coherence^{1,2} to exhibit Rabi oscillations when driven by a GHz microwave magnetic field tuned to the NV electron spin resonance (ESR) frequency f_0 .^{2,3} Increasing the NV Rabi oscillation frequency f_1 is often desired, because a larger f_1 for a given spin dephasing time allows a greater number of quantum-coherent manipulations.³ Since $f_1 = \gamma B_1/2^{1/2}$ where B_1 is the amplitude of the linearly driving microwave magnetic field and γ is the electron gyromagnetic ratio,³ obtaining a larger f_1 amounts to driving a conducting wire or antenna with a larger-amplitude GHz current to produce a stronger B_1 . However, increasing the driving current at GHz frequencies is generally a nontrivial task in microwave engineering.^{3–7}

Certain applications with NV electronic spins not only benefit from a high f_1 but actually require a minimum f_1 . A case in point is the measurement of nuclear magnetic resonance (NMR) signals—nuclear spin precession—using NV electronic spin dynamics as the detector.^{8–12} In this “NV-NMR” scheme, particularly in protocols based on pulsed dynamical decoupling, NV electronic spins can sense the frequency and phase of nuclear spin precession via dipole–dipole coupling, with the NV dynamics read out optically. A key requirement for such NV-NMR measurements is that f_1 must be significantly larger than the NMR frequency, f_{NMR} , i.e., the nuclear spin precession frequency. NV-NMR can offer higher

sensitivity for small samples than traditional inductive NMR, enabling spectroscopy at the nano and microscale.^{8–12} However, this advantage comes with the challenge that the requirement $f_1 > f_{\text{NMR}}$ becomes increasingly stringent as the static magnetic field B_0 is raised to achieve higher NMR spectral resolution. Since increasing B_0 raises both f_0 and f_{NMR} , the minimum f_1 required also increases. Meeting this requirement demands driving a conducting wire with a larger current amplitude at a higher GHz frequency (f_0), working against the general trend that microwave driving becomes more difficult at higher frequency. For this reason, the high-resolution NMR readily achieved with inductive readout, e.g., commercial 300–600 MHz ¹H NMR at $B_0 \approx 7.1$ –14.1 T, remains well beyond the current reach of NV-NMR.

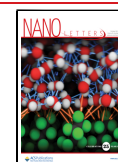
Thus, whether for NV-NMR or for other applications, substantial research has been devoted to increasing f_1 for NV electronic spins.^{3–7} In particular, large B_1 can be readily attained at GHz ESR frequencies using a wire loop, even without excessive current, at positions proximate to the wire

Received: July 23, 2025

Revised: September 26, 2025

Accepted: October 13, 2025

Published: October 16, 2025



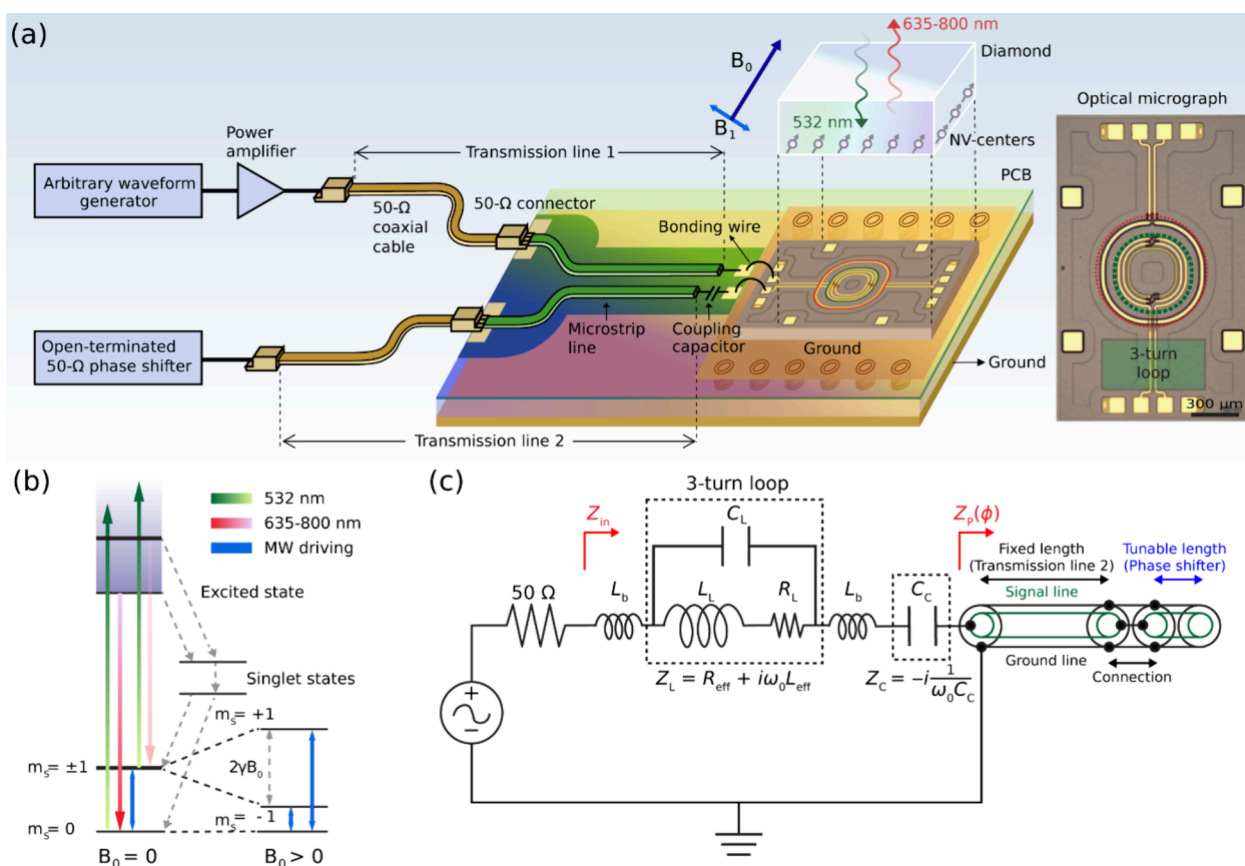


Figure 1. (a) Schematic of the device and measurement setup showing the full microwave path (left); optical image of the chip featuring the 3-turn planar Cu loop (right). The diamond is mounted on the chip so that its NV-rich $\sim 10 \mu\text{m}$ layer faces the loop. The 3-turn loop (dashed green circle, right) serves as the microwave antenna; the additional single loop (dashed red circle, right) is left open-circuited and unused. (b) NV electronic spin states, optical and microwave transitions, and dependence on B_0 . (c) Circuit model of the microwave path (Transmission line 1 is omitted, since the 50- Ω microwave source is matched to 50- Ω Transmission line 1). For maximal current delivery into the loop, $|Z_{in}|$ should be minimized (ideally to zero) by properly choosing C_C and ϕ .

rather than at the loop center. As an extreme example, exploiting such edge fields yielded $f_1 = 0.44 \text{ GHz}$ at $f_0 = 0.49 \text{ GHz}$ ($f_1/f_0 \approx 0.90$), albeit with significant B_1 inhomogeneity.³ These edge regions remain useful for applications involving a small number of NVs localized within $<1 \mu\text{m}$, but they are unsuitable for applications that require a spatially extended NV ensemble ($>1 \mu\text{m}$), such as micrometer-scale NV-NMR.^{8–12} For such applications, which demand greater B_1 and f_1 homogeneity, the loop center region is preferable; because B_1 is minimum at the center and increases radially outward, it is maximally homogeneous around the center. At the same time, because B_1 is lowest at the center, achieving a high target B_1 or f_1 is more difficult, requiring delivery of a larger-amplitude microwave current into the loop. For example, the work reported in ref 4 achieved millimeter-scale B_1 inhomogeneity of less than 5% (normalized standard deviation) at $f_0 = 2.87 \text{ GHz}$ in the loop center region, but the resulting f_1 value was only 14.3 MHz ($f_1/f_0 \approx 5.0 \times 10^{-3}$).

Here, we report strong yet homogeneous quantum-coherent manipulation of a large ensemble of NV electronic spins at GHz ESR frequencies, achieved through systematic microwave engineering that enhances the microwave current driving of a 3-turn planar loop coupled to a diamond (the “device”). Within a $40 \mu\text{m} \times 40 \mu\text{m}$ diamond area in the loop center region, we achieve $f_1 = 136.3 \text{ MHz}$ at $f_0 = 2.55 \text{ GHz}$ ($f_1/f_0 \approx 5.3 \times 10^{-2}$) with B_1 inhomogeneity of $\sim 1.5\%$ (normalized

standard deviation). This result supports our long-term aim of high-resolution NV-NMR spectroscopy at tesla-scale bias magnetic fields, since the demonstrated $40 \mu\text{m} \times 40 \mu\text{m}$ homogeneous region is on par with the analyte size of NV-NMR targets.^{10–12} Moreover, we demonstrate NV-ensemble-based detection of a $\sim 30 \text{ MHz}$ magnetic signal (similar to an NMR signal at $\sim 0.7 \text{ T}$ bias field) using the device.

Our device consists of a thin slab of diamond ($2.0 \text{ mm} \times 2.0 \text{ mm} \times 0.5 \text{ mm}$) mounted on four Cu support pads of a chip that features the 3-turn Cu microwave loop (Figure 1a, right). The support pads protrude slightly, leaving a micrometer-scale gap above the loop—unused in this work but available for future sample integration. The diamond slab fully covers the loop. We first describe the diamond sample and then the microwave loop. The surface of the diamond facing the loop embeds an ensemble of NV centers within a $\sim 10\text{-}\mu\text{m}$ depth. The NV-enriched layer is grown using chemical vapor deposition with isotopically purified ^{15}N and contains 99.99% ^{12}C ($\sim 0.01\%$ ^{13}C) and 17 ppm ^{15}N , yielding $\sim 2.7 \text{ ppm}$ of NV^- concentration. The measured NV electron spin dephasing times are $\sim 7.1 \mu\text{s}$ for a Hahn-Echo sequence and $\sim 33.0 \mu\text{s}$ for an XY8-6 sequence. In a static (bias) magnetic field, B_0 , two ESR frequencies arise: $f_0 = \Delta + \gamma B_0$ for the $m_s = 0 \leftrightarrow +1$ transition, and $f_0 = |\Delta - \gamma B_0|$ for the $m_s = 0 \leftrightarrow -1$ transition, with $\Delta \approx 2.87 \text{ GHz}$ due to the zero-field splitting (Figure 1b). The microwave drive can be tuned to either ESR transition to

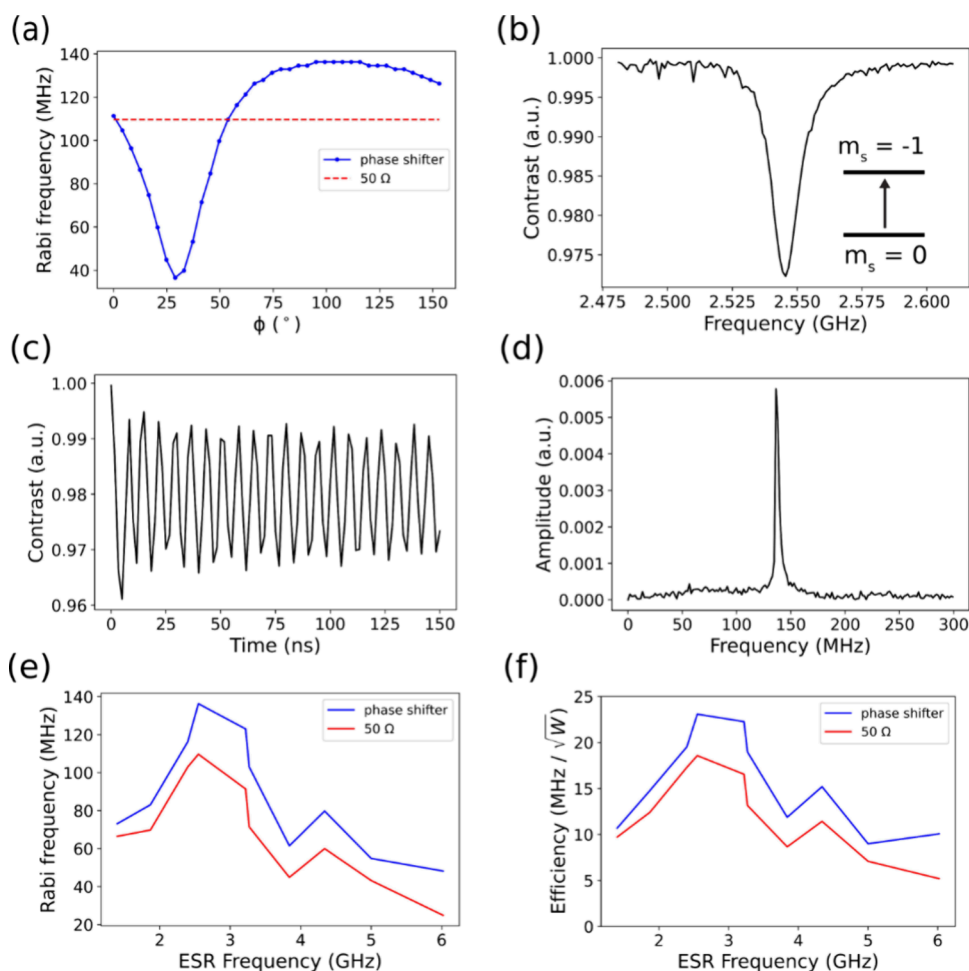


Figure 2. (a) NV-measured f_1 at the loop center vs ϕ (blue) and with fixed 50- Ω termination (red), at $f_0 = 2.55$ GHz for the splitting between $m_s = 0$ and $m_s = -1$ ($B_0 = 116$ G). At $\phi \approx 100^\circ$, f_1 is maximized at 136.3 MHz. (b–d) Example ODMR spectrum, Rabi oscillation, and Fourier transform of the Rabi oscillation with a single peak at $f_1 = 136.3$ MHz, all for $\phi \approx 100^\circ$ and $f_0 = 2.55$ GHz. (e) Maximum f_1 at the loop center obtained by ϕ tuning (blue) in comparison to f_1 at fixed 50- Ω termination (red) for a number of different f_0 values between 1.40 GHz and 6.02 GHz. (f) Repetition of (e) for driving efficiency, defined as the ratio of f_1 to the square root of the output power from the power amplifier.

induce Rabi oscillations between the corresponding NV spin states. In our setup, the NV centers have their quantization axis tilted 54.7° relative to the chip normal, and all values of B_0 and B_1 given throughout this paper are referenced to this NV axis: B_0 is the projection of the permanent-magnet field onto the NV axis (hence, tunable by adjusting the magnet's position and orientation); B_1 is the projection of the loop-produced microwave field onto the plane perpendicular to the NV axis. Optical initialization of NV spins into the $m_s = 0$ state, and subsequent optical readout of Rabi oscillations during microwave driving, follow standard protocol (Figure 1b; see the Methods section in the Supporting Information; also see Figure S1 for the optics setup).^{10–12}

We now describe the 3-turn loop. The 3 Cu turns (diameters 300 μm , 360 μm , and 420 μm ; width 17 μm ; effective thicknesses of 3 μm , ~ 9 μm , and ~ 9 μm ; turn-to-turn gap = 13 μm ; see Figure S2) are realized within a metallization stack framework, largely embedded in dielectric atop a 75- μm -thick semi-insulating SiC substrate, with partial exposure to air. The bottom of the chip is finished with a 10- μm -thick Au layer. The loop chip is designed by us, fabricated at a foundry, and packaged by us (see the Methods section).

The equivalent circuit of the loop (Figure 1c, dashed box) consists of an inductance L_L in series with a parasitic resistance

R_L with this series branch in parallel with a parasitic capacitance C_L . The dominant contribution to C_L is expected to come from interturn coupling, although smaller parasitic capacitances (e.g., to ground) are effectively absorbed into C_L . This simplified model largely reproduces the loop behavior observed in simulations (Figure S3). The self-resonance frequency of the loop is $f_{\text{SRF}} = (2\pi)^{-1}(L_L C_L)^{-1/2}$ and the loop impedance at the excitation frequency is $Z_L = (R_L + i\omega_0 L_L) \parallel (i\omega_0 C_L)^{-1} \equiv R_{\text{eff}} + i\omega_0 L_{\text{eff}}$ where $L_{\text{eff}} \approx L_L [1 - (\omega_0/\omega_{\text{SRF}})^2]^{-1}$ and $R_{\text{eff}} \approx R_L [1 - (\omega_0/\omega_{\text{SRF}})^2]^{-2}$ are the frequency-dependent effective loop inductance and resistance ($\omega_0 = 2\pi f_0$; $\omega_{\text{SRF}} = 2\pi f_{\text{SRF}}$). For efficient operation, $f_0 < f_{\text{SRF}}$ should hold, under which the inductive (L_L) branch dominates and the loop behaves inductively ($L_{\text{eff}} > 0$), efficiently generating the microwave magnetic field. In contrast, for $f_0 > f_{\text{SRF}}$, the capacitive (C_L) branch dominates, the loop becomes capacitive ($L_{\text{eff}} < 0$), and magnetic field generation becomes inefficient. Fewer turns increase f_{SRF} by reducing C_L but weakens B_1 for a given current. The chosen 3-turn loop geometry balances this tradeoff, with the loop diameter further chosen to balance field strength against homogeneity.

Simulations (Figure S3) yield $L_L \approx 4.25$ nH, $R_L \approx 3.0$ Ω , and $C_L \approx 0.23$ pF, together with $f_{\text{SRF}} \approx 5.1$ GHz. Thus, the main excitation frequency in this work, $f_0 = 2.55$ GHz, lies

below $f_{\text{SRF}} \approx 5.1$ GHz. At $f_0 = 2.55$ GHz, $Z_L \approx 5.4 + 90.7i \Omega$ with $R_{\text{eff}} \approx 5.4 \Omega$ and $L_{\text{eff}} \approx 5.7$ nH, which is inductive as expected, with a quality factor $Q = \omega_0 L_{\text{eff}}/R_{\text{eff}} \approx 17$. Of note, the chip also includes an additional single loop surrounding the 3-turn loop (Figure 1a, right), designed as a secondary shim. However, when driven, it coupled strongly to the primary loop, so it is left open-circuited and unused. Simulations confirm that in this open state, it has negligible effect on the primary loop (Figure S3).

The full microwave signal path is shown in Figure 1a, with its circuit model in Figure 1c. The chip with the diamond on top is mounted on a printed circuit board (PCB). One end of the loop is wire-bonded to “Transmission line 1” (a 50- Ω PCB microstrip plus a 50- Ω coaxial cable) connected to a microwave source (an arbitrary waveform generator followed by a 50- Ω power amplifier, ZHL-25W-63+). The other loop end is wire-bonded to a coupling capacitor C_C in series with “Transmission line 2” (another 50- Ω PCB microstrip plus another 50- Ω coax) connected to an open-terminated 50- Ω phase shifter. The chip’s gold backside is glued to the PCB ground plane.

In the circuit model (Figure 1c), the input impedance seen by the source is $Z_{\text{in}} = R_{\text{eff}} + i\omega_0(2L_b + L_{\text{eff}}) - i(\omega_0 C_C)^{-1} + Z_p(\phi)$, where L_b is the inductance of each bond wire, estimated as $L_b \approx 1$ nH, and $Z_p(\phi)$ is the impedance presented by Transmission line 2 (with fixed phase delay ϕ_0) plus the open-terminated phase shifter with a tunable phase delay ϕ . If Transmission line 2 and the phase shifter are lossless, $Z_p(\phi) = -iZ_0 \cot(\phi + \phi_0)$ ($Z_0 = 50 \Omega$), which spans $-\infty$ to $+\infty$ as ϕ varies, although, in practice, losses limit the span. The goal is then to choose C_C and ϕ to minimize $|Z_{\text{in}}|$ (ideally to zero; intentionally mismatched from the source 50- Ω impedance) to maximize microwave current into the loop and, hence, f_1 . At $f_0 = 2.55$ GHz, simulations estimate $R_{\text{eff}} + i\omega_0(2L_b + L_{\text{eff}}) \approx 5.4 + 123i \Omega$, so choosing $C_C = 0.5$ pF makes its capacitance impedance $-i(\omega_0 C_C)^{-1}$ nearly cancel the simulated 123i Ω inductive term, yielding $Z_{\text{in}} \approx 5.4 - 2.1i + Z_p(\phi)$. If ϕ is then tuned so that $Z_p(\phi) \approx 2.1i$, Z_{in} becomes purely real, minimizing $|Z_{\text{in}}|$ to 5.4 Ω .

In this ideal consideration, where L_b and L_{eff} are assumed known a priori so that C_C cancels the inductive impedance almost exactly (from 123i Ω to $-2.1i \Omega$), $Z_p(\phi)$ tuning would not be essential. One could simply ground the far side of the coupling capacitor and accept $Z_{\text{in}} \approx 5.4 - 2.1i$, giving $|Z_{\text{in}}| = 5.8 \Omega$, which is already close to the theoretical minimum of 5.4 Ω . In practice (including our present case), however, L_b and L_{eff} cannot be predicted with perfect accuracy. Achieving near-zero cancellation of the inductive impedance with C_C alone is therefore challenging, and the residual reactance may be substantially greater than $-2.1i$ and not negligible. In this situation, $Z_p(\phi)$ tuning provides a valuable adjustment, allowing residual reactance to be nulled and $|Z_{\text{in}}|$ minimized.

Moreover, $Z_p(\phi)$ tuning extends the operational range of f_0 around 2.55 GHz. Because C_C is fixed at 0.5 pF (optimized for $f_0 = 2.55$ GHz), the imbalance between inductive and capacitive impedances grows as f_0 deviates from 2.55 GHz. In such case, $Z_p(\phi)$ supplies the additional reactive impedance needed to cancel the mismatch and minimize $|Z_{\text{in}}|$, provided the mismatch lies within the finite span of $Z_p(\phi)$ set by losses in Transmission line 2 and the phase shifter.

Figure 2a shows NV measurements of f_1 at the loop center vs ϕ (blue), juxtaposed with f_1 measured at the loop center with a fixed 50- Ω load replacing the phase shifter (red; see Figure S4

for its circuit diagram), where $f_0 = 2.55$ GHz for the $m_s = 0 \leftrightarrow -1$ transition ($B_0 = 116$ G in the present experiment). The ϕ scan yields f_1 values both above and below the fixed-load f_1 value, demonstrating that $|Z_{\text{in}}|$ —and, thus, delivered current—varies widely with ϕ (see Figure S5 for impedance measurements). At $\phi \approx 100^\circ$, f_1 reaches the maximum of 136.3 MHz, a notably high NV Rabi frequency measured at the loop center (Table S1). At this ϕ value, which minimizes $|Z_{\text{in}}|$, $Z_p(\phi)$ removes the residual reactance that $C_C = 0.5$ pF could not fully cancel.

Under the optimal $\phi \approx 100^\circ$ at $f_0 = 2.55$ GHz, Figure 2b shows the NV optically detected magnetic resonance (ODMR) spectrum (i.e., optically detected ESR spectrum) while Figure 2c shows a representative Rabi oscillation; Figure 2d displays the Fourier transform of the Rabi oscillation with a single peak at $f_1 = 136.3$ MHz (see Figure S6 for different f_0 values). The ~ 3 MHz ^{15}N hyperfine splitting (Figure S7) is power-broadened and unobserved in Figure 2b; and neither of the two associated detuned Rabi frequencies differ from $f_1 = \gamma B_1 / 2^{1/2} = 136.3$ MHz by less than 0.05%, because $f_1 \gg 3$ MHz, so they merge into a single f_1 peak in Figure 2d.

Figure 2e plots the maximum f_1 (Rabi frequency) at the center of the loop obtained by ϕ tuning alongside f_1 with a fixed 50- Ω load for a number of f_0 values between 1.40 and 6.02 GHz. As at $f_0 = 2.55$ GHz, optimal tuning drives a faster Rabi oscillation than the fixed-load case. The corresponding driving efficiency, defined as the ratio of f_1 to the square root of the output power from the power amplifier, is likewise higher for the optimally tuned configuration for all tested f_0 (Figure 2f; see also Figure S8). Figure 2e shows that, as f_0 moves away from 2.55 GHz, f_1 tends to decrease because $C_C = 0.5$ pF is optimized for $f_0 = 2.55$ GHz and residual mismatch between inductive and capacitive impedances at f_0 other than 2.55 GHz may exceed the finite span of $Z_p(\phi)$. Also, note that f_1 is substantially smaller for f_0 beyond $f_{\text{SRF}} \approx 5.1$ GHz, as expected.

At $f_0 = 2.55$ GHz, with the ϕ tuned for the maximal f_1 of 136.3 MHz at the loop center, the 3-turn loop delivers not only strong but also homogeneous microwave B_1 around the loop center. Figure 3a shows the f_1 map (equivalently a B_1 map, since $f_1 \propto B_1$) measured with the NV ensemble across a 280 $\mu\text{m} \times 280 \mu\text{m}$ area surrounding the innermost turn, using a scanned 5- μm diameter laser spot and a 10- μm pixel pitch. Within a 40 $\mu\text{m} \times 40 \mu\text{m}$ central region, B_1 shows little inhomogeneity, and measured NV Rabi oscillations at each point within this area are slowly damped, with Fourier spectra displaying a single, sharp peak (Figure S9). Across a larger 100 $\mu\text{m} \times 100 \mu\text{m}$ region (Figure 3b), B_1 variations increase, with Rabi oscillations more rapidly damped and Fourier spectra correspondingly broadened, at each measurement point outside the 100 $\mu\text{m} \times 100 \mu\text{m}$ area (Figure S9). Quantitatively, the mean f_1 is 139.3 and 150.3 MHz, with normalized standard deviations of about 1.5% and 6.3% within the 40 $\mu\text{m} \times 40 \mu\text{m}$ and 100 $\mu\text{m} \times 100 \mu\text{m}$ areas, respectively (Figure 3c). This B_1 homogeneity within the 40 $\mu\text{m} \times 40 \mu\text{m}$ NV-diamond area is expected to be sufficient for high-resolution, tesla-scale NV-NMR spectroscopy of a picoliter-scale analyte.^{10–15} Equivalent measurements at $f_0 = 6.02$ GHz, above the loop’s self-resonance frequency f_{SRF} , are shown in Figure S10.

Finally, we use our device to detect a 29.992 MHz radio frequency (RF) magnetic field signal generated by a test coil to emulate a tesla-scale NMR signal. The RF test signal is measured by the NV ensemble using coherently averaged

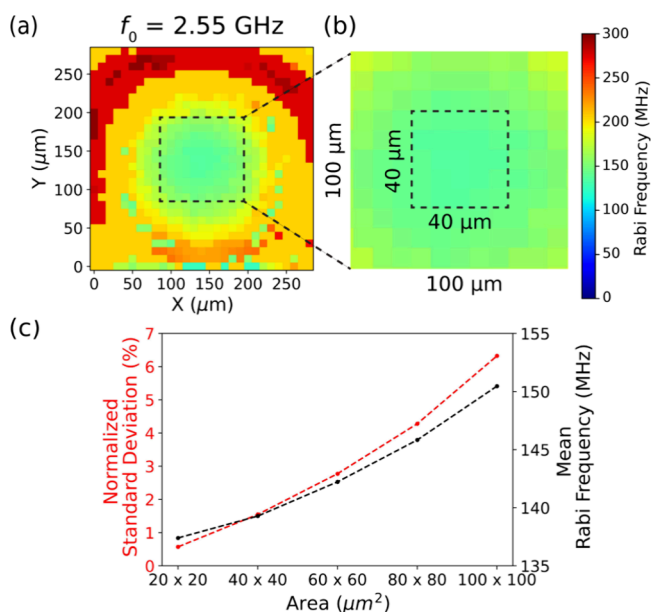


Figure 3. (a) NV-measured map of f_1 across a $280 \mu\text{m} \times 280 \mu\text{m}$ area surrounding the innermost turn at $f_0 = 2.55 \text{ GHz}$, with ϕ tuned for the maximal f_1 of 136.3 MHz at the loop center. (b) Zoomed $100 \mu\text{m} \times 100 \mu\text{m}$ area (dashed box in panel (a)). (c) Mean and normalized standard deviation of f_1 vs window size centered on the loop center with $f_0 = 2.55 \text{ GHz}$, obtained from the f_1 map in panel (a). The normalized standard deviation is about 1.5% within the $40 \mu\text{m} \times 40 \mu\text{m}$ region.

synchronized readout (CASR),^{10,11} a quantum spectroscopy protocol that alternates dynamical decoupling and optical readout of the NV electronic spins to provide Hz-scale spectral resolution (Figure 4a). We perform the measurements at $f_0 = 2.55 \text{ GHz}$ ($B_0 = 116 \text{ G}$), with optimal phase (ϕ) tuning yielding the maximum f_1 of 136.3 MHz , which is sufficiently large to enable phase-coherent measurements of the 29.992 MHz RF test signal.^{8–12} The NV CASR measurement uses an XY8-6 sequence with a central frequency $f_{\text{CASR}} \approx 30 \text{ MHz}$. The CASR protocol effectively down-converts the RF signal frequency, and we observe an oscillatory variation in NV photoluminescence (PL) intensity at the down-converted frequency of $\delta f \approx 30 \text{ MHz} - 29.992 \text{ MHz} = 8 \text{ kHz}$. The Fourier transform of observed PL time-domain signal (Figure 4b, left), measured for 1 s , shows a signal peak at 8.008 kHz (Figure 4b, right), with the 8 Hz deviation from 8 kHz being well less than the 1 ppm error of the RF signal generator (Rigol, Model DG 1032). Increasing the CASR measurement time from 1 s to 10 s to 100 s , the spectral resolution of the RF test signal improves from about 1 Hz to 0.1 Hz to 50 mHz , eventually limited by drift in the system (Figure S11).

This work demonstrates an approach to realize high Rabi frequency for a dense NV ensemble at the micrometer scale, with good spatial homogeneity, by increasing a microwave magnetic field in the center of a multiturn wire loop with careful microwave engineering, instead of relying on proximity to the loop. Specifically, at an NV driving frequency of 2.55 GHz ($B_0 = 116 \text{ G}$), we achieve a 136.3 MHz NV Rabi frequency with 1.5% inhomogeneity over a $40 \mu\text{m} \times 40 \mu\text{m}$ diamond area. We demonstrate the utility of our approach by using the NV ensemble in this diamond area to detect a $\sim 30\text{-MHz}$ magnetic signal with Hz-scale spectral resolution. This capability may benefit high Rabi frequency applications that

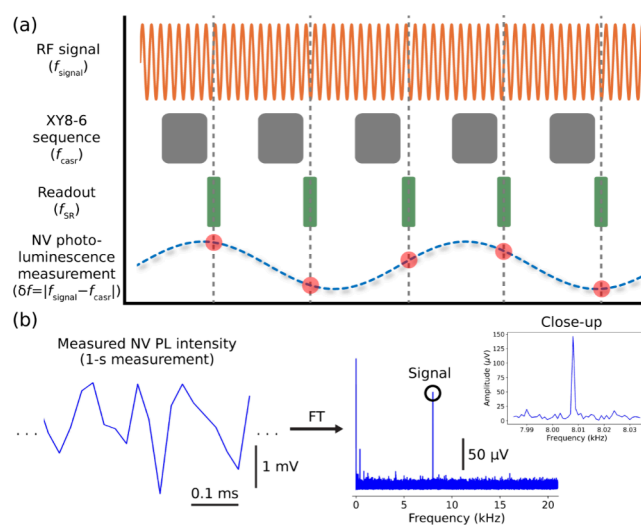


Figure 4. (a) CASR timing diagram for NV ensemble detection of a 29.992-MHz (f_{signal}) RF magnetic field from a test coil. NV electronic spins are driven at $f_0 = 2.55 \text{ GHz}$ ($B_0 = 116 \text{ G}$)—with the maximal f_1 of 136.3 MHz —using alternating application of an XY8-6 dynamical decoupling sequence and NV PL readout. The CASR protocol produces an oscillatory variation in NV PL at frequency $\delta f = f_{\text{signal}} - f_{\text{CASR}}$ where $f_{\text{CASR}} \approx 30 \text{ MHz}$ is the central frequency used in the XY8-6 sequence. (b) Example measured NV PL intensity trace (left) and its Fourier transform (right), showing a peak at 8.008 kHz , in good agreement with expectations given the 1 ppm error of the signal generator used in this measurement.

employ a micrometer-scale ensemble of NV electronic spins, such as tesla-scale NV-NMR, although significant additional engineering challenges remain for NV-NMR at such high bias magnetic fields. In envisioned future work, a driver amplifier will be custom-designed with a microwave loop in the same chip and will be fabricated using a high-bandgap semiconductor (e.g., GaN) technology, such that the microwave current is further increased due to both the short distance between the active and passive circuits and also their codesign.

ASSOCIATED CONTENT

Supporting Information

The Supporting Information is available free of charge at <https://pubs.acs.org/doi/10.1021/acs.nanolett.5c03811>.

Methods, comparison of device used in present work to several other works in the literature, optical setup for NV excitation and detection, experimental setup, simulation of the 3-turn primary loop with and without the open-circuited outer secondary loop, circuit model of the microwave signal pathway using the $50\text{-}\Omega$ termination, 1-port s -parameter measurement and impedance analysis, NV ODMR and Rabi oscillation measurements at various f_0 values, ODMR spectrum under low microwave power at $f_0 = 2.52 \text{ GHz}$, output power of the ZHL-25W-63+ power amplifier as a function of microwave excitation frequency, f_1 measurements at varying distances from the center of the 3-turn loop for the NV-measured maps of f_1 at $f_0 = 2.55 \text{ GHz}$ and $f_0 = 6.02 \text{ GHz}$, determination of the spectral resolution for the CASR measurement shown in Figure 4 at varying measurement times (PDF)

AUTHOR INFORMATION

Corresponding Authors

Donhee Ham – John A. Paulson School of Engineering and Applied Sciences, Harvard University, Cambridge, Massachusetts 02138, United States; Email: donhee@seas.harvard.edu

Ronald L. Walsworth – Quantum Technology Center, University of Maryland, College Park, Maryland 20742, United States; Department of Physics, Joint Quantum Institute, and Department of Electrical and Computer Engineering, University of Maryland, College Park, Maryland 20742, United States; Email: walsworth@umd.edu

Authors

Han Sae Jung – John A. Paulson School of Engineering and Applied Sciences, Harvard University, Cambridge, Massachusetts 02138, United States; orcid.org/0000-0003-3251-9790

Johannes Cremer – Quantum Technology Center, University of Maryland, College Park, Maryland 20742, United States

Aoyang Zhang – John A. Paulson School of Engineering and Applied Sciences, Harvard University, Cambridge, Massachusetts 02138, United States; School of Integrated Circuits, Tsinghua University, Beijing 100084, China; Present Address: For Aoyang Zhang : now with School of Integrated Circuits, Tsinghua University, Beijing 100084, China

Shuhao Fan – John A. Paulson School of Engineering and Applied Sciences, Harvard University, Cambridge, Massachusetts 02138, United States

Sangha Kim – John A. Paulson School of Engineering and Applied Sciences, Harvard University, Cambridge, Massachusetts 02138, United States

Guang Yang – John A. Paulson School of Engineering and Applied Sciences, Harvard University, Cambridge, Massachusetts 02138, United States; Present Address: For Guang Yang; now with the Anlyan Center, Yale University School of Medicine, New Haven, CT 06519, USA.

Complete contact information is available at:

<https://pubs.acs.org/10.1021/acs.nanolett.5c03811>

Author Contributions

○Authors H.S.J., J.C., and A.Z. contributed equally to this work. D.H. and R.L.W. conceived the work. H.S.J., J.C., S.K., and S.F. performed the experiments. A.Z. designed the 3-turn loop and the PCB. S.F. and A.Z. performed the s-parameter simulations. J.C., H.S.J., and A.Z. put together the measurement setup. H.S.J. and G.Y. packaged the chip. D.H. and R.L.W. supervised the project. H.S.J., J.C., A.Z., R.L.W., and D.H. wrote the manuscript, and all authors read and discussed it.

Notes

The authors declare no competing financial interest.

ACKNOWLEDGMENTS

This work was supported by the Gordon and Betty Moore Foundation, under Contract No. 7797.01; the Advanced Research Projects Agency-Energy (ARPA-E; Program Directors, Dr. Isik Kizilyalli and Dr. Olga Spahn), under Contract No. DE-AR0001063; the U.S. Army Research Laboratory, under Contract No. W911NF2420143; and the University of Maryland Quantum Technology Center.

REFERENCES

- (1) Balasubramanian, G.; Neumann, P.; Twitchen, D.; Markham, M.; Kolesov, R.; Mizuochi, N.; Isoya, J.; Achard, J.; Beck, J.; Tessler, J.; et al. Ultralong spin coherence time in isotopically engineered diamond. *Nat. Mater.* **2009**, *8*, 383–387.
- (2) Bar-Gill, N.; Pham, L. M.; Jarmola, A.; Budker, D.; Walsworth, R. L. Solid-state electronic spin coherence time approaching one second. *Nat. Commun.* **2013**, *4*, 1743.
- (3) Fuchs, G. D.; Dobrovitski, V. V.; Toyli, D. M.; Heremans, F. J.; Awschalom, D. D. Gigahertz dynamics of a strongly driven single quantum spin. *Science* **2009**, *326*, 1520–1522.
- (4) Bayat, K.; Choy, J.; Baroughi, M. F.; Meesala, S.; Loncar, M. Efficient, uniform, and large area microwave magnetic coupling to NV centers in diamond using double split-ring resonators. *Nano Lett.* **2014**, *14* (3), 1208–1213.
- (5) Sasaki, K.; Monnai, Y.; Saijo, S.; Fujita, R.; Watanabe, H.; Ishi-Hayase, J.; Itoh, K. M.; Abe, E. Broadband, large-area microwave antenna for optically detected magnetic resonance of nitrogen-vacancy centers in diamond. *Rev. Sci. Instrum.* **2016**, *87*, 053904.
- (6) Mariani, G.; Nomoto, S.; Kashiwaya, S.; Nomura, S. System for the remote control and imaging of MW fields for spin manipulation in NV centers in diamond. *Sci. Rep.* **2020**, *10*, 4813.
- (7) Yaroshenko, V.; Soshenko, V.; Vorobyov, V.; Bolshedvorskii, S.; Nenasheva, E.; Kotelnikov, I.; Akimov, A.; Kapitanova, P. Circularly polarized microwave antenna for nitrogen vacancy centers in diamond. *Rev. Sci. Instrum.* **2020**, *91*, 035003.
- (8) Mamin, H. J.; Kim, M.; Sherwood, M. H.; Rettner, C. T.; Ohno, K.; Awschalom, D. D.; Rugar, D. Nanoscale nuclear magnetic resonance with a nitrogen-vacancy spin sensor. *Science* **2013**, *339*, 557–560.
- (9) Staudacher, T.; Shi, F.; Pezzagna, S.; Meijer, J.; Du, J.; Meriles, C. A.; Reinhard, F.; Wrachtrup, J. Nuclear magnetic resonance spectroscopy on a (5-nanometer)³ sample volume. *Science* **2013**, *339*, 561–563.
- (10) Glenn, D. R.; Bucher, D. B.; Lee, J.; Lukin, M. D.; Park, H.; Walsworth, R. L. High-resolution magnetic resonance spectroscopy using a solid-state spin sensor. *Nature* **2018**, *555*, 351–354.
- (11) Bucher, D. B.; Glenn, D. R.; Park, H.; Lukin, M. D.; Walsworth, R. L. Hyperpolarization-enhanced NMR spectroscopy with femtomole sensitivity using quantum defects in diamond. *Phys. Rev. X* **2020**, *10*, 021053.
- (12) Arunkumar, N.; Olsson, K. S.; Oon, J. T.; Hart, C. A.; Bucher, D. B.; Glenn, D. R.; Lukin, M. D.; Park, H.; Ham, D.; Walsworth, R. L. Quantum logic enhanced sensing in solid-state spin ensembles. *Phys. Rev. Lett.* **2023**, *131*, 100801.
- (13) Mousoulis, C.; Xu, X.; Reiter, D. A.; Neu, C. P. Single cell spectroscopy: noninvasive measures of small-scale structure and function. *Methods* **2013**, *64*, 119–128.
- (14) Grisi, M.; Vincent, F.; Volpe, B.; Guidetti, R.; Harris, N.; Beck, A.; Boero, G. NMR spectroscopy of single sub-nL ova with inductive ultra-compact single-chip probes. *Sci. Rep.* **2017**, *7*, 44670.
- (15) Grant, S. C.; Aiken, N. R.; Plant, H. D.; Gibbs, S.; Mareci, T. H.; Webb, A. G.; Blackband, S. J. NMR spectroscopy of single neurons. *Magn. Reson. Med.* **2000**, *44*, 19–22.